LANGMUIR

pubs.acs.org/Langmuir Article

Director Distortion and Phase Modulation in Deformable Nematic and Smectic Liquid Crystal Spheroids

Sepideh Norouzi, Rui Zhang, Juan G. Munguia-Fernández, Luis de Pablo, Ye Zhou, Nader Taheri-Qazvini, Harrison Shapiro, Samuel Morin, Jose A. Martinez-Gonzalez,* Monirosadat Sadati,* and Juan J. de Pablo*

Cite This: *Langmuir* 2022, 38, 15272−15281 Read Online

ACCESS | Metrics & More | Article Recommendations | Supporting Information

ABSTRACT: The growing interest in integrating liquid crystals (LCs) into flexible and miniaturized technologies brings about the need to understand the interplay between spatially curved geometry, surface anchoring, and the order associated with these materials. Here, we integrate experimental methods and computational simulations to explore the competition between surface-induced orientation and the effects of deformable curved boundaries in uniaxially and biaxially stretched nematic and smectic microdroplets. We find that the director field of the nematic LCs upon uniaxial strain reorients and forms a larger twisted defect ring to adjust to the new deformed geometry of the stretched droplet. Upon biaxial extension, the director field initially twists in the now oblate geometry and subsequently transitions into a uniform vertical orientation at high strains. In smectic microdroplets, on the other hand, LC alignment transforms from a radial smectic layering to a quasi-flat layering in a compromise between interfacial and dilatation forces. Upon removing the mechanical strain, the smectic LC recovers its initial radial configuration; however, the oblate geometry traps the nematic LC in the metastable vertical state. These findings offer a basis for the rational design of LC-based flexible devices, including wearable sensors, flexible displays, and smart windows.

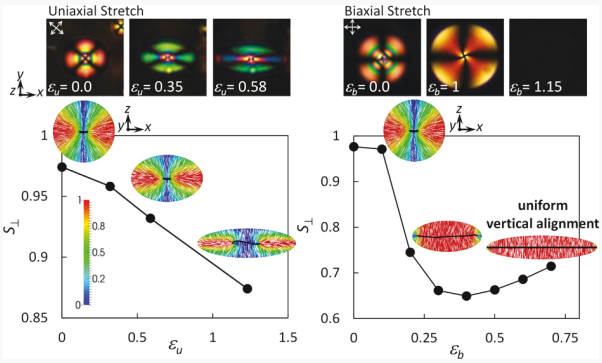

INTRODUCTION

In liquid crystal (LC)-based devices, the interplay among confinement geometry, anchoring condition, and elastic constant is key to defining a system's preferred orientation field and response behavior.[1−9] Understanding the orientation and ordering transitions within such materials in curved boundaries is therefore central to developing emerging LC-based miniaturized curved and flexible devices, including wearable sensors and flexible displays. Confinement within curved boundaries, as in micro- or nanodroplets, is known to distort the LC director field due to incompatibility between the preferred director field alignment and the curvature of the space, resulting in the emergence of new defect structures.[10−17] Depending on the type of surface anchoring, LC molecules in a spherical nematic microdroplet, for example, adopt two distinct director field configurations. A bipolar configuration with two-point defects at the poles (boojums) appears when the interface induces planar anchoring. In contrast, a radial morphology with a point-like defect at the center of the nematic droplet is formed when the interface produces a homeotropic alignment. The interfacial tension, bulk elasticity, and the level of confinement have also been found to influence the director field orientation in nematic and smectic LCs.[10,14,16−19] By tuning the bend-to-splay elastic constant ratio, for example, Jiang and Yang observed a transition from a bipolar to a toroidal director orientation in nematic droplets with a tangential boundary condition.[16] Erdmann et al. found a radial to axial ordering transition in nematic LC droplets upon reducing the droplet size.[20] Janus microdroplets as another exotic topological confinement can be a host to a variety of LC configurations.[21−23] In Janus smectic microdroplets composed of silicone oil and 8CB, Wei et al. reported various stable and metastable configurations, including dislocation rings, focal conic domains, and undulations induced by the coupling of curvature and homeotropic surface anchoring.[21]

Nematic LCs confined in shells, toroids, cylindrical capillaries, and coaxial capillaries have also been explored experimentally and computationally.[10−12,24−32] They exhibit a variety of fascinating structures, including an escaped radial structure in a cylinder with homeotropic anchoring and planar polar with two-line defects (defect, +1/2) along the major

Received: September 7, 2022
Revised: November 11, 2022
Published: December 1, 2022

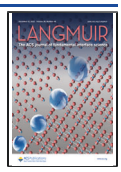

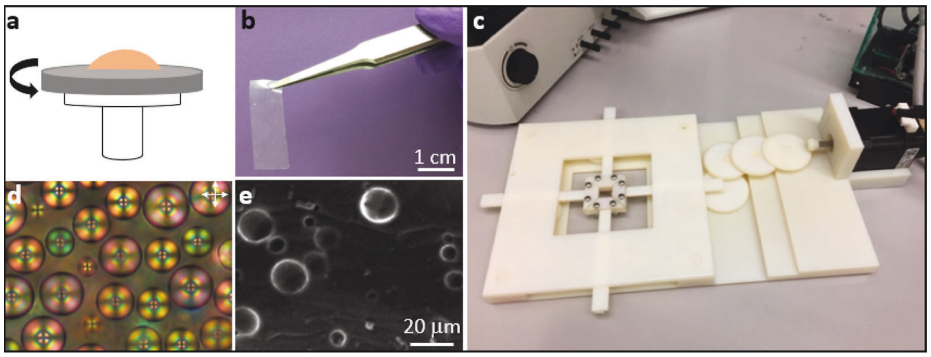

Figure 1. Dispersed LC droplets in the PDMS film. (a) Spin coating of the PDMS/LC mixture, (b) PDLC film, (c) uniaxial and biaxial stretching devices, (d) cross-polarized optical micrograph of the radial configuration of polydisperse nematic 5CB droplets in PDMS film, and (e) SEM micrograph of the cross-section of the prepared PDLC.

cylindrical axis.[24−28] In coaxial cylinders and toroids, on the other hand, the interplay of concave and convex curvatures and large saddle-splay contributions results in double-twisted configurations.[29,30] In shells, a radial configuration has been observed in nematic LCs with uniform homeotropic surface alignment. Upon transition to planar surface alignment, however, various defect configurations emerged, including half hyperbolic hedgehogs, half radial hedgehogs, and four defects with a topological surface charge of +1/2 in thin shells.[10−12,24] Confining smectic LCs in shells with homeotropic boundary conditions, on the other hand, tiles the shell surface with polygonal focal conic domains, which transition to a set of spherical lune patterns under planar surface anchoring.[31,32]

The effect of topological curvature on the director field configuration of nematic and smectic LCs has also been studied in the context of polymer-dispersed LC (PDLC) films, where micrometer-sized LC droplets are dispersed in a solid transparent polymer matrix.[33−38] PDLC materials have found a wide range of applications in display technologies, smart windows, and optical strain gauges that can be prepared using microencapsulation and phase-separation techniques. In the former method, the LC droplets are dispersed in a water-soluble polymer solution such as polyvinyl alcohol, and a PDLC is obtained after water evaporation. In the latter, the LC is mixed with monomeric precursors of a polymer, and LC droplets phase separate from the matrix upon polymerization of the monomers.

PDLC films also provide a useful platform to study the orientational morphology of nematic LCs in response to external stimuli, such as electric fields, magnetic fields, and mechanical strain, all of which have significant practical importance.[39−45] For example, by continuously changing the aspect ratio of the bipolar droplet upon the uniaxial extension of PDLC films, the spherical LC domains become ellipsoidal, exhibiting different optical characteristics than the spherical ones. It has been shown that the initial droplet shape, surface anchoring strength, and the phase at which droplets are stretched determine the orientational ordering of the prolate droplets and their optical properties.[39−42] The effect of spheroid shape and curvature on the reconfiguration of nematic LCs has also been the subject of theoretical and numerical studies. According to Abukhdeir and co-workers, nematic LCs in oblate and prolate cavities adopt a director field with a defect ring, whose size is controlled by surface geometry and anchoring as well as external fields.[43,44] When exposed to an electric field, the reorientation of the LC molecules in prolate cavities with planar surface anchoring has been shown to occur at higher field strengths than in spherical droplets. On the other hand, LC molecules with tilted surface anchoring in oblate cavities exhibited a lower field threshold and a faster electrical response than those with planar anchoring, making them suitable for various electro-optical applications.[45]

More generally, the effect of curvature on the ordering transition and topological defects of LCs has been studied extensively for geometries with planar surface anchoring. Few studies have examined the ordering transition of nematic and smectic LCs upon continuous curvature evolution of homeotropic boundaries. We are aware of the experimental work by Jeong et al., who studied the topological defects of smectic 4-octyl-4′-cyanobiphenyl (8CB) LC in prolate spheroids and elliptic cylindrical geometries with homeotropic anchoring.[46,47] They reported a point-to-line defect transition in prolate spheroids and focal conic domain formation in elliptic cylindrical confinement as the cavity is stretched and the aspect ratio increases. In another study, Goyal and Denn used simulated annealing to calculate the minimum free energy landscape of nematic spheroids. They found that surface-directed forces control the LC morphology in elongated droplets with homeotropic surface alignment.[48]

In this work, upon continuous and reversible uniaxial and biaxial extension of the PDLC film, we deform nematic and smectic LC microdroplets with homeotropic boundary conditions into prolate and oblate spheroids, respectively. We integrate experimental techniques and computational simulations to understand the effects of mechanical strain and curvature of the resulting new geometries on the structural and ordering transitions, including defect formation and optical features, for both nematic 5CB and smectic 8CB LCs. Since 8CB in prolate spheroids with homeotropic anchoring has already been studied,[46] we briefly discuss the corresponding results in the Supporting Information (Figure S1).

MATERIALS AND METHODS

Nematic 4-pentyl-4-cyanobiphenyl (5CB) and smectic 4-octyl-4′-cyanobiphenyl (8CB) LCs were purchased from Sigma-Aldrich. LC droplets were dispersed in a polydimethylsiloxane (PDMS) polymer film to induce homeotropic anchoring. To do so, the LCs were dissolved in the silicone elastomer (base/curing agent of 10:1—Sylgard 184, Dow Corning) and hexane (co-solvent) with weight percentages of 5, 85, and 10%, respectively. After spin-casting of the

https://doi.org/10.1021/acs.langmuir.2c02461
Langmuir 2022, 38, 15272−15281

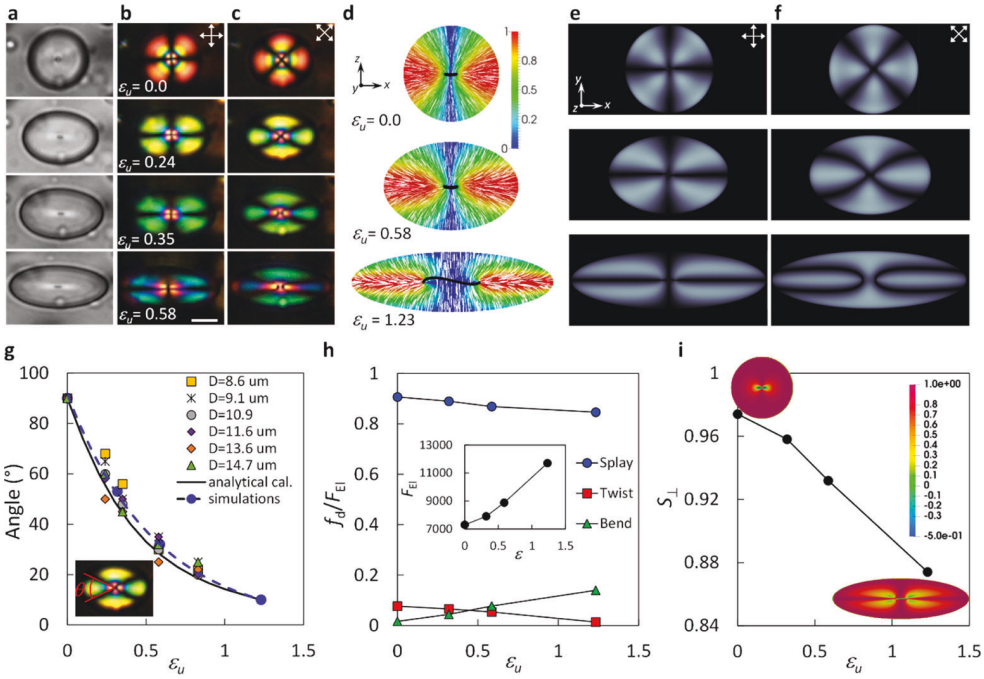

Figure 2. Uniaxial deformation of a nematic LC droplet with radial surface anchoring. (a) Bright field. (b) Transmission-mode cross-polarized images of a stretched droplet at different values of uniaxial strain, ε_u. (c) Polarized images of the droplet when the cross-polarizers are rotated by 45°. (d) Director fields and (e,f) crossed-polarized micrographs of a stretched nematic LC droplet obtained from Landau-de Gennes simulations. (g) The acute angle between the black cross when the cross-polarizers are oriented by 45° as a function of strain obtained from the experiment, analytical calculation, and computer simulations. (h) Contribution of the distortion-free energies (f_d), splay, twist, and bend, to the total free energy, F_{El}, of the uniaxially stretched system obtained by mean-field simulations. Inset shows the total elastic free energy, which increases as the system is strained. (i) Average orthogonal order parameter ($S_\perp$) as a function of uniaxial strain. The images show lateral views of the deformed nematic droplet, and the color bar corresponds to the local value of $S_\perp$.

solution on a glass substrate, the LC droplets were phase-separated from PDMS over the polymerization and solvent evaporation processes at room temperature (Figure 1a). For the uniaxial and biaxial deformations, rectangular film strips with dimensions of 10 × 20 mm and square films with dimensions of 20 × 20 mm were cut out from the 150 μm thick PDLC sheets (Figure 1b). To deform the PDLC films, we designed and three-dimensionally printed a mechanical unit capable of stretching the PDLC films both uniaxially and biaxially at a fixed speed of 150 μm/s (Figure 1c). The PDLC samples were stretched under an optical microscope at room temperature, where 5CB and 8CB are in the nematic and smectic phases, respectively. Before stretching, PDLC films were heated to an isotropic phase (T_{5CB} = 40 °C, T_{8CB} = 45 °C) to clear unavoidable mounting-induced deformations and director field reconfigurations. In fact, the mounting-induced reconfigurations were mainly observed in 8CB droplets. Due to the fast structural relaxation (a few milliseconds) of 5CB LC, no permanent structural changes were noted in 5CB droplets over the mounting process.[49] We utilized an Olympus BX51 optical microscope equipped with crossed polarizers to track the defect configuration of the 5CB and 8CB droplets upon deformation of the PDLC film. Isolated droplets were selected to avoid interference of transmitted wavelengths of the surroundings in the crossed-polarized images and accurately determine the structural evolution.

At a theoretical level, we modeled the confined LC using a Landau-de Gennes formalism,[50,51] where the free energy of the LC, F, is given in terms of the tensor order parameter, $\mathbf{Q}$, defined by $Q_{ij} = S\,(n_i\,n_j - 1/3\,\delta_{ij})$, with i, j = 1, 2, 3, and n_i are the x, y, z components of the local director vector. S is the scalar order parameter. The free energy functional is given by

$$F(\mathbf{Q}) = \int \mathrm{d}^3x[f_\mathrm{p}(\mathbf{Q}) + f_\mathrm{E}(\mathbf{Q})] + \int \mathrm{d}^2x f_\mathrm{S}(\mathbf{Q}) \tag{1}$$

where f_P accounts for the bulk contribution, f_E corresponds to the elastic distortions, and f_S is the surface contribution to the free energy. They are given by

$$f_\mathrm{p} = \frac{A}{2}\left(1 - \frac{U}{3}\right)\mathrm{tr}(\mathbf{Q}^2) - \frac{AU}{3}\mathrm{tr}(\mathbf{Q}^3) + \frac{AU}{4}\mathrm{tr}(\mathbf{Q}^2)^2 \tag{2a}$$

$$f_\mathrm{E} = \frac{1}{2}\left[L_1\frac{\partial Q_{ij}}{\partial x_k}\frac{\partial Q_{ij}}{\partial x_k} + L_2\frac{\partial Q_{jk}}{\partial x_k}\frac{\partial Q_{jl}}{\partial x_l}\right] \tag{2b}$$

$$f_\mathrm{S}^\mathrm{P} = W_\mathrm{P}(\tilde{\mathbf{Q}} - \tilde{\mathbf{Q}}^\perp)^2 \tag{2c}$$

$$f_\mathrm{S}^\mathrm{H} = \frac{1}{2}W_\mathrm{H}(\mathbf{Q} - \mathbf{Q}^0)^2 \tag{2d}$$

In eq 2a, A and U are phenomenological parameters that depend on temperature and pressure;[50−52] in eq 2b L_i's are the elastic constants. Equations 2c and 2d correspond to the surface contributions to the free energy for planar degenerate and homeotropic anchoring, respectively. In eq 2c, W_P is the planar anchoring energy, $\tilde{\mathbf{Q}} = \mathbf{Q} + S\boldsymbol{I}/3$ and $\tilde{\mathbf{Q}}^\perp = \boldsymbol{P}\tilde{\mathbf{Q}}\boldsymbol{P}$, $\boldsymbol{P}$ is the projection operator $P_{ij} = \delta_{ij} - \nu_i\nu_j$ and $\boldsymbol{\nu}$ is the vector normal to the surface. In eq 2d, W_H is the homeotropic anchoring energy, and $\mathbf{Q}^0$ is a surface-preference tensor order parameter.

Minimization of the free energy, which leads to metastable and stable states, was achieved using the Ginzburg−Landau relaxation method, where $\mathbf{Q}$ evolves toward equilibrium according to[50,51]

$$\frac{\partial \mathbf{Q}}{\partial t} = -\frac{1}{\gamma}\left[\boldsymbol{\Pi}\left(\frac{\delta F}{\delta \mathbf{Q}}\right)\right] \tag{3}$$

with boundary conditions such that $\boldsymbol{\Pi}[(\delta F/\delta\nabla\mathbf{Q})\cdot\boldsymbol{\nu}] = 0$, where $\boldsymbol{\Pi}(\boldsymbol{B}) = 1/2(\boldsymbol{B} + \boldsymbol{B}^\mathrm{T}) - 1/3\mathrm{tr}(\boldsymbol{B})\boldsymbol{I}$ ensures the symmetric and traceless properties of the $\mathbf{Q}$-tensor parameter and γ is a diffusion

https://doi.org/10.1021/acs.langmuir.2c02461
Langmuir 2022, 38, 15272−15281

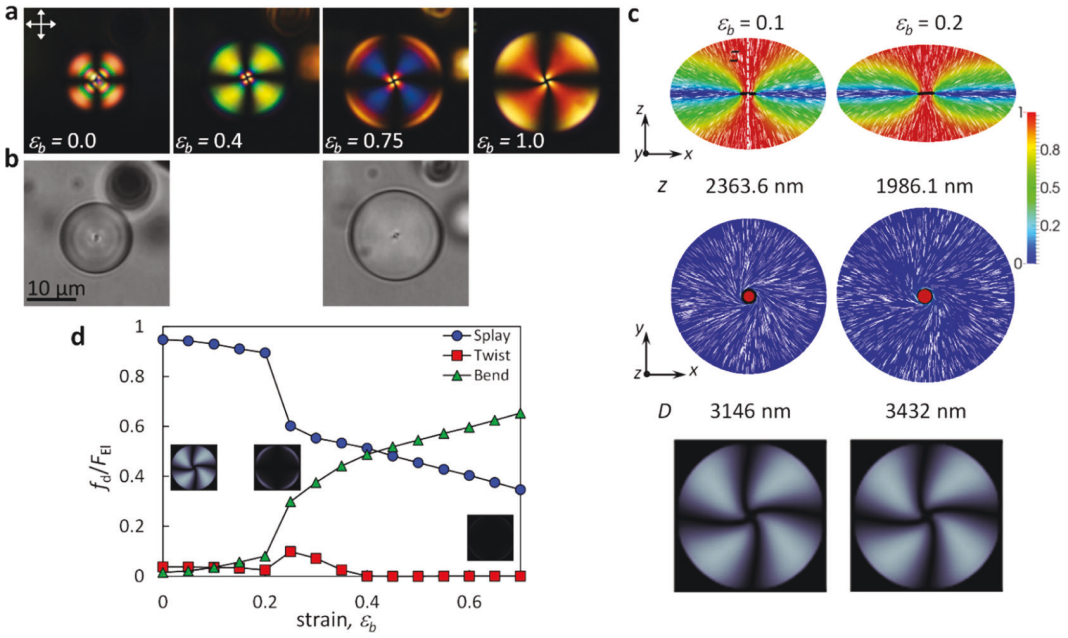

Figure 3. Biaxial deformation of a nematic LC droplet with homeotropic surface anchoring. (a) Transmission-mode crossed-polarized micrographs and (b) bright-field images of a stretched 5CB droplet at different values of biaxial strain, $\varepsilon_b = (A - A_0)/A_0$, where A is the surface area of a droplet in the $x-y$ plane after biaxial deformation, and A_0 is the surface area of the initial droplet in the relaxed state. (c) Top and side views of the director fields as well as polarized light micrographs of a stretched nematic LC droplet obtained from Landau-de Gennes simulations at two strain values. (d) Contribution of distortion-free energies (f_d), splay, twist, and bend, to the total elastic free energy, F_{El}, of the biaxially stretched system obtained by mean-field simulations. Insets correspond to simulations of representative crossed-polarized images at different strains.

coefficient. For the systems considered here, we use $W = 4 \times 10^{-3}$ J m^{-2} (for homeotropic and planar anchoring), $U = 3.5$, which corresponds to $S = \frac{1}{4}\left(1 + 3\sqrt{1 - \frac{8}{3U}}\right) = 0.616$, and the elastic constants $L_1 = \frac{1}{2S^2}\left[K_{22} + \frac{1}{3}(K_{33} - K_{11})\right]$, $L_2 = \frac{1}{S^2}(K_{11} - K_{22} - K_{24})$ with $K_{11} = K_{33} = 2K_{22}$, and $K_{24} = 0$. For the minimization of the free energy functional, we use a finite difference method with a lattice array having a mesh resolution of $\xi = \sqrt{\frac{L_1}{A}} \approx 7.15$ nm.

Simulations of the cross-polarizer images were obtained based on the Jones-matrix formalism, which takes into account the change in the polarization and phase shift of the light when passing through the system: the polarizer, the liquid crystal, and the analyzer. Additional details can be found in ref 53.

RESULTS AND DISCUSSION

The nematic and smectic LC droplets (5CB and 8CB) were phase-separated from the PDMS monomeric precursors over the polymerization process and formed primarily spherical geometries (Figure 1d,e). The distinct Maltese cross-like pattern and a core point defect in the cross-polarized micrograph of the PDLC film confirm the radial configuration of 5CB and 8CB LC droplets induced by the PDMS polymer matrix (Figure 1d).

When uniaxial tension is applied to the PDLC film, the spherical droplet cavities gradually deform within the polymer film and turn into prolate ellipsoids with their major axes oriented along the stretch direction. While the alignment of the LC molecules in spherical geometry is governed by the interplay between surface anchoring and bulk elasticity, the variation of the boundary's curvature also plays an important role in elliptic geometry. The uniaxial extension can lead to a major conflict between the surface-imposed homeotropic anchoring and the bulk orientation in the regions between the minor and major axes. Upon uniaxial stretching, the interface parallel to the stretching direction is enlarged, interfering with the formation of a radial orientation and inducing new defect structures (Figure 2a–c).

In situ bright-field and crossed-polarized optical microscopy were used to study the structural reorganization of the 5CB molecules in the nematic phase upon uniaxial extension (Figure 2a–c). The magnitude of the applied uniaxial strain, ε_u was defined along the long axis using $\varepsilon_u = (b - D_0)/D_0$, where b is the long axis of the deformed droplet and D_0 is the diameter of the initial droplet in the relaxed state. The birefringence images were captured for cases where the stretched axis was aligned at 0 and 45° to the polarizer (Figure 2b,c). In the 0° position, the relative orientation of the extinction lines upon extension remains similar to that in the non-deformed state. However, it exhibits strong strain dependency when the major axis is positioned at 45° to the polarizer (Figure 2c). The angle between the extinction lines was measured from the cross-polarized images, which can also be described using $\theta = 2\tan^{-1}(b/a)$, where a and b are the short and long axes of the ellipsoid, respectively (Figure 2g). In fact, upon uniaxial extension, the alignment of the LC molecules in the prolate cavity with homeotropic anchoring is governed by the interplay between surface curvature, anchoring strength, and bulk elastic constants. At low deformations, the stretched droplet in the polymer film retains the radial configuration, and the central point defect remains unchanged. At large aspect ratios, on the other hand, the homeotropic anchoring and the anisotropic prolate geometry break the radial symmetry, leading to a larger defect region (Figure 2c).

We used the Landau-de Gennes formalism to calculate the free energy of the system and define the preferred alignment of the LC molecules at large strains. Our results indicate that the orientation dynamics in prolate nematic LC with homeotropic

https://doi.org/10.1021/acs.langmuir.2c02461
Langmuir 2022, 38, 15272−15281

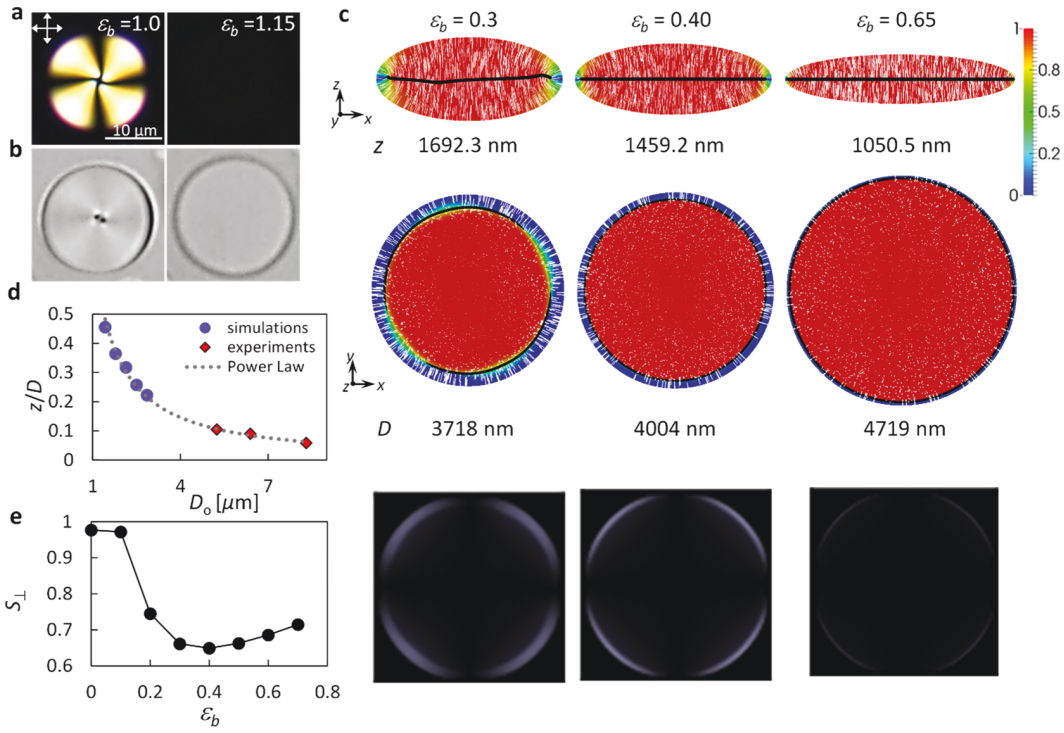

Figure 4. Transition from twisted configuration to uniform vertical alignment in oblate nematic LC. (a) Transmission-mode crossed-polarized and (b) bright-field images of an oblate nematic LC showing the transition from the twisted structure to the uniform vertical arrangement at ε_b = 1.15. (c) Lateral and top views of the director alignment for three representative cases of the biaxially stretched system for the high strain range. The radius of the Saturn ring grows with the strain and becomes comparable to the radius of the oblate. The director field inside the ring shows a uniform vertical alignment. (d) Normalized thickness of the droplet at which the transition from the twisted configuration to uniform vertical alignment occurs as a function of initial droplet size. (e) Average orthogonal nematic order parameter ($S_\perp$) as a function of strain.

surface anchoring strongly depends on the geometry and aspect ratio, in agreement with our experimental observations. It is worth mentioning that the single defect point observed at the center of the nematic droplet in the experimental images appears as a small defect ring in simulations (Saturn ring) (Figure 2d). The ring is located in the region with the highest elastic distortions. Upon uniaxial deformation, the director field of the LC molecules reorients, forming a larger defect ring to adjust to the new boundary conditions of the stretched geometry (Figure 2d). Larger ring defects are more susceptible to the system's fluctuations and can twist at a lower cost. A theoretical study by Chiccoli et al.[54] has also reported a distinct increase in the ring defect radius as radially aligned nematic droplets deviate from a cylindrical symmetry.

We obtained the cross-polarized images of the stretched droplets from Landau-de Gennes simulations and calculated the variation of the acute angle between the extinction lines at the 45° orientation to the polarizer. Our results are in quantitative agreement with the experimental observations (Figure 2e,f and circle-dashed line in Figure 2g).

The distortion-free energy f_d was also analyzed as a function of strain for a nematic droplet. It elucidates that splay deformation remains dominant in the radially oriented nematic droplet, regardless of the deformation magnitude. However, the bend distortion is favored in the low strain regime (ε < 0.5). Overall, stretching the radial droplet enhances the total elastic free energy of the system (Figure 2h, inset). Finally, knowing the radial symmetry variation versus strain, the orthogonal component of the nematic scalar order parameter, $S_\perp$, was calculated for uniaxially stretched nematic droplets using[48]

$$S_\perp = \frac{1}{N}\left\langle \sum_{i=1}^{N}\left[\frac{3}{2}(\boldsymbol{n}_i\cdot\boldsymbol{r}_i)^2 - \frac{1}{2}\right]\right\rangle$$

where N is the number of lattice nodes inside the spheroid and $\boldsymbol{r}_i$ is the normal vector to the spheroid surface located at the i-node. In the relaxed state (ε = 0), $S_\perp \approx 1$ for a radial configuration (when $\boldsymbol{n}_i \| \boldsymbol{r}_i$), and it reduces significantly upon uniaxial extension as the director field deviates from a radial-like symmetry (Figure 2i).

Upon biaxial extension, the radially oriented nematic LC droplets become increasingly oblate; the curvature decreases on the top surface of the droplet, whereas it increases on the side. This variation in the curvature of the boundaries within the PDMS film significantly influences the alignment of the LC molecules. According to the experimental cross-polarized micrographs, as a radial 5CB droplet is biaxially stretched, the internal alignment of the LC molecules transforms from radial to a new structure in which the director conformations are twisted (Figure 3a,b). The transition from radial to twisted morphologies occurs due to the continuous reordering of the nematic LC molecules upon biaxial extension. In agreement with our experimental observations, computational simulations reveal a twisted director field inside a biaxially stretched nematic LC droplet. The side and top views of a droplet at two different strains and their corresponding cross-polarized images clearly depict the twisted configuration, in agreement with our experiments (Figure 3c).

From an energetic point of view, any distortion of the director field can increase the system's free energy. Calculating the elastic energy of a biaxially stretched droplet can help us

https://doi.org/10.1021/acs.langmuir.2c02461
Langmuir 2022, 38, 15272−15281

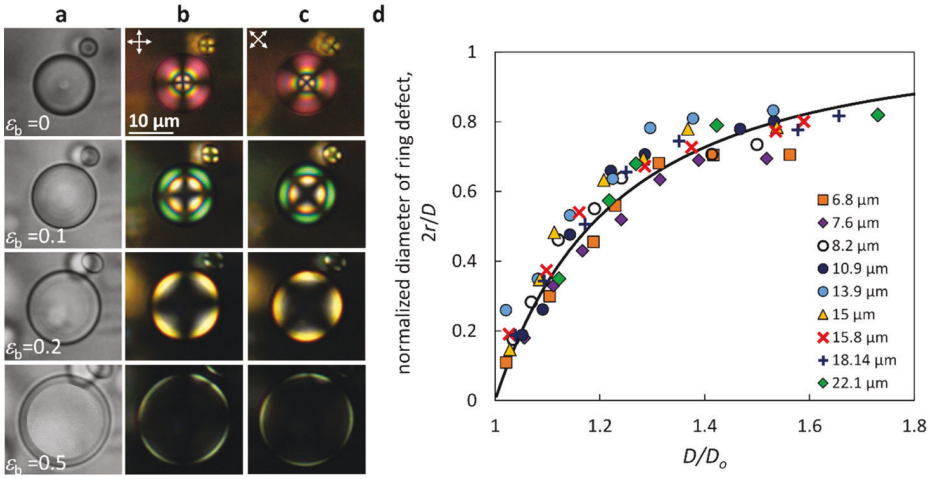

Figure 5. Biaxial deformation of a smectic LC droplet with homeotropic surface anchoring. (a) Bright-field and (b) transmission-mode crossed-polarized images of a biaxially stretched droplet at different strain values. (c) Crossed-polarized images of the droplet when the cross-polarizers are rotated by 45°. (d) Normalized diameter of the ring defect as a function of stretch ratio (the diameter of the defect area is normalized to the diameter of the biaxially stretched droplet).

determine the ground state of the system. The contributions of each of the distortion-free energies (f_d) (splay, twist, and bend) to the total free energy, F_{El}, of the biaxially stretched droplet can also be extracted from mean-field simulations (Figure 3d). In the small (or zero) strain regime, where the splay distortion is dominant, the system shows a twist-like configuration. The twist configuration is also observed in the spherical droplets when the droplet size is below 4 μm (Figure S2).

At higher stretch ratios, the strong spatial constraint in the z-direction strains the director field and spontaneously reorients and aligns the LC molecules in the 5CB droplets vertically to the surface throughout the entire thickness. This sharp transition of the director field from twisted to uniform vertical alignment entirely blocks the light passing through the cross-polarizer (Figure 4a,b). The director field transition to a uniform vertical configuration at high biaxial strains is also confirmed by our computational simulations. Depending on the droplet size, the strain at which the radius of the ring defect (Saturn ring) suddenly expands and becomes comparable to the radius of the oblate particle may vary (Figure 4c). As the Saturn ring grows, it divides the deformed droplet into two regions with distinct molecular alignments. While the director field inside the ring adopts a uniform vertical alignment, the bend deformation enhances significantly at the periphery of the oblate, which has been delimited by the oblate's surface and the Saturn ring (Figure 4c). The side and top views of a droplet at three different strains and their corresponding crossed-polarized images clearly depict the evolution of the ring defect and the uniform vertical alignment of the LC director field inside the ring. The normalized thickness of the droplet at which the transition from the twisted configuration to uniform vertical alignment takes place was determined for a range of droplet sizes. The experimental and simulation results show a power law decay for the magnitude of the normalized thickness with droplet size. This suggests that the larger the droplet, the higher the biaxial strain required to trigger the transition from the twisted radial alignment to the uniform vertical configuration (Figure 4d). We also calculated the orthogonal component of the nematic scalar order parameter as a function of strain for a biaxially stretched nematic droplet. As expected, $S_\perp \sim 1$ for the relaxed state with radial configuration, while it decreases considerably for an oblate geometry. After the transition to the uniform vertical configuration at the oblate central region, $S_\perp$ increases again with further biaxial deformation as the vertically aligned region expands through the oblate (Figure 4e).

Smectic LC. When smectic 8CB droplets are dispersed in the PDMS matrix, they adopt a spherical concentric packing (Figure S1) with an ideal radial orientation where the defect is localized at the center (Figure 5a–c). Deforming an 8CB spherical droplet to an oblate upon biaxial extension of the PDMS matrix reorients the LC molecules in the smectic phase, leading to the nucleation and growth of a ring defect in the central part. As we continue biaxially extending the now oblate 8CB, the curvature of the system increases at the periphery, gradually expanding the defect ring to an extent comparable to the oblate size. Inside the ring, the layering configuration of the smectic LC undergoes a transition from a radial to a parallel arrangement, starting from the central part of the droplet. Since 8CB molecules in layers are aligned vertically to the respective stretching directions, this region appears dark under the crossed polarizer. On the periphery of the droplet, however, the distribution of the director field remains radial, which is confirmed by the characteristic extinction cross when the cross-polarizers are rotated by 45°. The extinction lines follow the orientation of the polarizer and analyzer, indicating the radial nature of the LC configuration on the periphery. This transition from radial to normal alignment is essentially a consequence of the gradual reorientation of the 8CB molecules, which occurs due to the geometrical confinement.

We studied the evolution and growth behavior of the ring defect upon biaxial extension by quantifying the size of the ring for a range of droplet sizes. Since the dimension of the droplet in the z-axis is not directly accessible, we plotted the defect growth versus stretch ratio instead of the aspect ratio used by Jeong and Kim.[46] The normalized diameter of the ring defect (normalized to the diameter of the oblate, D) as a function of stretch ratio (D/D_o, D_o is the diameter of the droplet at the initial state where $\varepsilon_b = 0$) exhibits fast growth for small stretch ratios, which levels off at high D/D_o. Additionally, these results

https://doi.org/10.1021/acs.langmuir.2c02461
Langmuir 2022, 38, 15272−15281

indicate that the evolution of the ring defects is almost independent of the initial droplet size.

This behavior can be attributed to the tendency of the biaxially stretched smectic LC with a layered structure to adopt a different geometry inside the PDMS polymer matrix. As we biaxially stretch an 8CB droplet, the layering configuration transitions from concentric rings to a parallel arrangement at the central part. This makes the interaction between the LC layers stronger than the PDMS−LC interfacial tension, which leads to the formation of a nearly flat top surface (Figure 6).

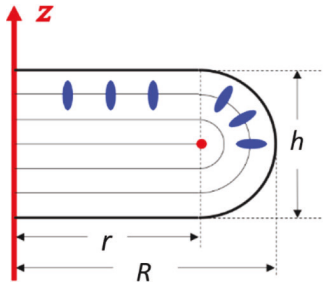

Figure 6. Illustration of the geometry of a stretched 8CB droplet. The shape is rotationally symmetric with respect to the *z*-axis.

For 8CB, its interfacial tension is about $\sigma = 10$ dyn/cm,[21,22] and its dilation energy is $B = 10^8$ dyn/cm^2.[55] The critical length scale at which interfacial energy is comparable to dilation energy is $l_c = \sigma/B = 1$ nm. The average droplet size $R_0 = 10\ \mu$m $\gg l_c$, implying that the dilation energy (BR_0^3) is much higher than the interfacial energy (σR_0^2), leading to high interfacial deformation. This supports our picture that an 8CB droplet under biaxial stretch will adopt a faceted shape.

According to the energy argument, an 8CB droplet under biaxial extension deforms into a shape having flat top and bottom surfaces, as illustrated in Figure 6. The shape is rotationally symmetric with respect to the *z*-axis, and the rotating surface consists of a rectangle and a semicircle. By introducing the radius of the ring defect *r*, the initial droplet radius R_0 and the stretched droplet radius *R*, one can use volume conservation to arrive at a relation between *r* and $h = 2(R-r)$

$$hr^2 + \frac{\pi}{4}h^2 r + \frac{h^3}{6} - \frac{4}{3}R_0^3 = 0$$

By solving the above equation, one can plot the relation between the normalized defect diameter $2r/D$ and stretch rate D/D_0, which is shown with a solid dark line in Figure 5d and is in good agreement with the experimental data.

The formation of a flat, faceted top surface has been reported for an 8CB droplet deposited on a flat substrate with strong homeotropic anchoring. In fact, a faceted geometry with a flat top surface and curved edges is formed to satisfy the parallel alignment of the LC layers. This structure has been observed in smectic B and blue-phase LCs, as well as in symmetric diblock copolymers.[56,57]

Mechanical Reorientation and Relaxation of Oblate 5CB and 8CB. When the mechanical force is gradually removed from the oblate 5CB and 8CB LCs with uniform alignment, the director field reorients under the internal kinetics of the droplet to recede from its initial strain-free radial

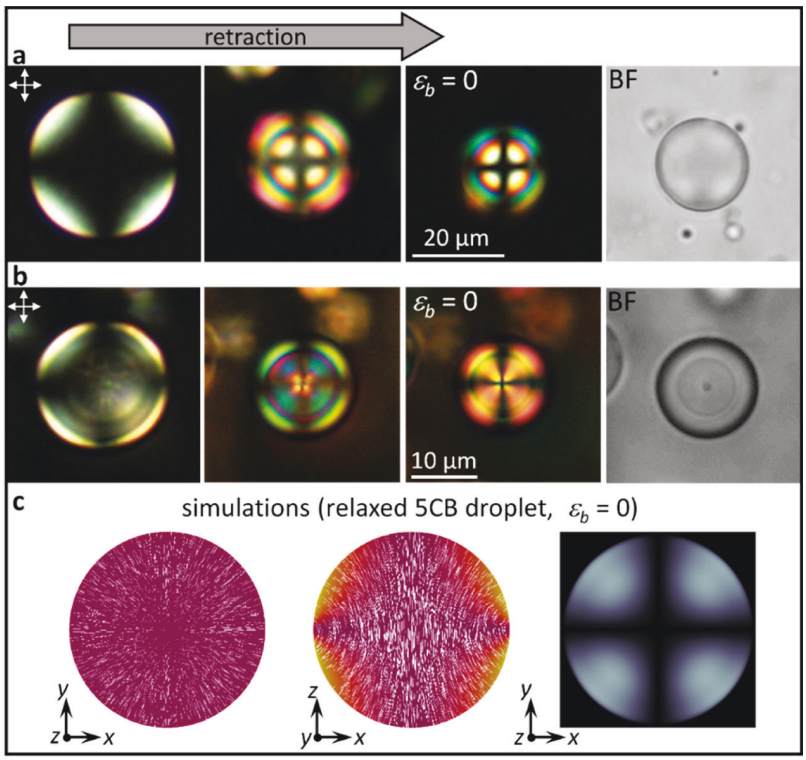

Figure 7. Relaxation (retraction) of 5CB and 8CB droplets upon mechanical stress release. Transmission-mode cross-polarized images of the relaxation processes of the (a) 5CB droplet and (b) 8CB droplet. The bright-field images indicate that the 5CB droplet never recovers its initial radial configuration. (c) Top and lateral views of the director alignment, as well as the simulated cross-polarized image of a relaxed 5CB droplet, elucidate that the oblate geometry traps the nematic director field configuration in a metastable state.

https://doi.org/10.1021/acs.langmuir.2c02461
Langmuir 2022, 38, 15272−15281

configuration. While the 8CB droplet resumes its radial orientation at room temperature, the absence of a point defect at the center of the strain-free 5CB droplet indicates that its initial radial configuration is never recovered (Figure 7). Although the radial configuration develops from the droplet's surface toward the center, the central region never transforms into the radial alignment. In other words, the biaxial deformation of the nematic LC droplet to oblate geometry kinetically traps the alignment of the director field in a metastable state.

CONCLUSIONS

In this work, we have used experimental measurements and computational simulations to investigate the ordering reconfiguration of nematic 5CB and smectic 8CB LCs upon uniaxial and biaxial mechanical deformation. The 5CB and 8CB were dispersed in a PDMS polymer film to induce homeotropic anchoring at the microdroplet interface. The PDLCs were obtained through the phase separation of the LCs from PDMS during the polymerization process. We found that the anisotropic deformation of 5CB upon uniaxial extension breaks the radial director symmetry, forming an axial-like director ordering with a twisted defect ring at the center. Upon biaxial extension, the 5CB microdroplets adopt the twisted director confirmation, which transitions to a uniform vertical orientation at high strain. The contribution of the distortion-free energies (splay, bend, and twist) obtained from mean-field simulations demonstrates that the biaxial extension of 5CB droplets favors the bend distortion while penalizing other modes. In contrast, the splay contribution is always dominant in the uniaxially stretched nematic LC microdroplets. The biaxial extension of 8CB microdroplets, on the other hand, transforms the radial layered conformation into a quasi-flat layered system due to the compromise that must be attained between interfacial and dilatation forces. And finally, our results show that the biaxially stretched 8CB microdroplets recover the radial orientation when the mechanical strain is removed. However, the oblate geometry kinetically traps 5CB in a metastable state.

Overall, this work highlights that the interplay between surface anchoring, curvature, mechanical deformation, and bulk elasticity can lead to new molecular arrangements and optical responses. This fundamental understanding could help pave the way for the design of LC devices, including smart windows, flexible displays, sensors, and mechano-optical metamaterials.

AUTHOR CONTRIBUTIONS

M.S., J.A.M.-G., and J.J.de P. conceived the work. S.N. and M.S. performed experiments. L.de P., H.S., and S.M. fabricated the stretching device. J.A.M.-G., R.Z., J.G.M., and Y.Z. conceived and performed numerical simulations and theoretical calculations. M.S. and N.T.Q. performed the SEM imaging. S.N., J.A.M.-G., R.Z., M.S., and J.J.de P. wrote the paper.

ASSOCIATED CONTENT

Supporting Information

The Supporting Information is available free of charge at https://pubs.acs.org/doi/10.1021/acs.langmuir.2c02461.

8CB in prolate spheroids with homeotropic surface anchoring and droplet size effect on the twisted configuration at zero strain (PDF)

AUTHOR INFORMATION

Corresponding Authors

Jose A. Martinez-Gonzalez − *Facultad de Ciencias, Universidad Autónoma de San Luis Potosí, San Luis Potosí 78295, México;* orcid.org/0000-0001-7257-8889; Email: jose.adrian.martinez@uaslp.mx

Monirosadat Sadati − *Department of Chemical Engineering, University of South Carolina, Columbia, South Carolina 29208, United States;* orcid.org/0000-0001-9701-9637; Email: sadati@cec.sc.edu

Juan J. de Pablo − *Pritzker School of Molecular Engineering, University of Chicago, Chicago, Illinois 60637, United States; Argonne National Laboratory, Lemont, Illinois 60439, United States;* orcid.org/0000-0002-3526-516X; Email: depablo@uchicago.edu

Authors

Sepideh Norouzi − *Department of Chemical Engineering, University of South Carolina, Columbia, South Carolina 29208, United States*

Rui Zhang − *Hong Kong University of Science & Technology, Kowloon 999077, Hong Kong;* orcid.org/0000-0002-2346-345X

Juan G. Munguia-Fernández − *Facultad de Ciencias, Universidad Autónoma de San Luis Potosí, San Luis Potosí 78295, México;* orcid.org/0000-0003-3794-3048

Luis de Pablo − *University of Chicago Laboratory Schools, Chicago, Illinois 60637, United States*

Ye Zhou − *Pritzker School of Molecular Engineering, University of Chicago, Chicago, Illinois 60637, United States;* orcid.org/0000-0002-4618-9318

Nader Taheri-Qazvini − *Department of Chemical Engineering, University of South Carolina, Columbia, South Carolina 29208, United States;* orcid.org/0000-0003-2114-7338

Harrison Shapiro − *University of Chicago Laboratory Schools, Chicago, Illinois 60637, United States*

Samuel Morin − *University of Chicago Laboratory Schools, Chicago, Illinois 60637, United States*

Complete contact information is available at: https://pubs.acs.org/10.1021/acs.langmuir.2c02461

Notes

The authors declare no competing financial interest.

ACKNOWLEDGMENTS

M.S. was supported by the NSF CAREER award 2146428 and NSF SC EPSCoR under grant 21-GE03. J.A.M.-G. acknowledges support from Ciencia de Frontera CONACYT grant CF-2019-74885 and computer resources, technical advice, and support provided by the Laboratorio Nacional de Supercómputo del Sureste de México (LNS), a member of the CONACYT National Laboratories, with Project 201901023N. J.J.dP. was supported by the Department of Energy, Basic Energy Sciences, Division of Materials Science, under grant DESC0019762.

REFERENCES

(1) Xie, S.; He, R.; Zhu, Q.; Jin, M.; Yang, R.; Shen, S.; Cui, J.; Zou, Y.; Zhang, M.; Shui, L. Label-free optical sensor based on liquid crystal sessile droplet array for Penicillin G determination. *Colloids Surf. A Physicochem. Eng. Asp.* **2022**, *644*, 128728.

(2) Esteves, C.; Ramou, E.; Porteira, A. R. P.; Moura Barbosa, A. J. M.; Roque, A. C. A. Seeing the Unseen: The role of liquid crystals in gas sensing technologies. *Adv. Opt. Mater.* **2020**, *8*, 1902117.
(3) Chuang, E. Y.; Ho, T. L.; Wang, Y. C.; Hsiao, Y. C. Smartphone and home-based liquid crystal sensor for rapid screening of acute myocardial infarction by naked-eye observation and image analysis. *Talanta* **2022**, *250*, 123698.
(4) Joralmon, D.; Alfarhan, S.; Kim, S.; Tang, T.; Jin, K.; Li, X. Three-dimensional printing of liquid crystals with thermal sensing capability via multi-materials vat polymerization. *ACS Appl. Polym. Mater.* **2022**, *4*, 2951−2959.
(5) Pagidi, S.; Park, H. S.; Lee, D. Y.; Kim, M. S.; Lee, S. H. Nanosize-confined nematic liquid crystals at slippery interfaces of polymer composites consisting of poly(hexyl methacrylate). *J. Mol. Liq.* **2022**, *350*, 118540.
(6) Song, M.; Seo, J.; Kim, H.; Kim, Y. Unltrasensitive multi-functional flexible sensors based on organic field-effect transistors with polymer-dispersed liquid crystal sensing layers. *Sci. Rep.* **2017**, *7*, 2630.
(7) Wu, K.; Sun, J.; Gao, L.; Xing, H.; Cai, M.; Zhao, T.; Yang, C.; Ye, W.; Kong, X. Highly sensitive and transparent flexible temperature sensor based on nematic liquid crystals. *Liq. Cryst.* **2022**, *49*, 372−379.
(8) Mbarak, H.; Hamidi, S. M.; Mohajerani, E.; Zaatar, Y. Electrically driven flexible 2D plasmonic structure based on nematic liquid crystal. *J. Phys. D* **2019**, *52*, 415106.
(9) Sadati, M.; Ramezani-Dakhel, H.; Bu, W.; Sevgen, E.; Liang, Z.; Erol, M.; Rahimi, M.; Taheri Qazvini, N.; Lin, B.; Abbott, N. L.; Roux, B.; Schlossman, M. L.; de Pablo, J. J. Molecular structure of canonical liquid crystal interfaces. *J. Am. Chem. Soc.* **2017**, *139*, 3841.
(10) Serra, F. Curvature and defects in nematic liquid crystal. *Liq. Cryst.* **2016**, *43*, 1920−1936.
(11) Sharma, A.; Jampani, V. S. R.; Lagerwall, J. P. F. Realignment of liquid crystals driven by temperature-dependent surfactant solubility. *Langmuir* **2019**, *35*, 11132−11140.
(12) Lopez-Leon, T.; Koning, V.; Devaiah, V.; Vitelli, A.; Fernandez-Nieves, A. Frustrated nematic order in spherical geometries. *Nat. Phys.* **2011**, *7*, 391−394.
(13) Sadati, M.; Zhou, Y.; Melchert, D.; Guo, A.; Martinez-Gonzalez, J. A.; Roberts, T. F.; Zhang, R.; de Pablo, J. J. Spherical nematic shells with a prolate ellipsoidal core. *Soft Matter* **2017**, *13*, 7465−7472.
(14) Wang, X.; Bukusoglu, E.; Abbott, N. L. A practical guide to the preparation of liquid crystal-templated microparticles. *Chem. Mater.* **2017**, *29*, 53−61.
(15) Miller, D. S.; Wang, X.; Abbott, N. L. Design of functional materials based on liquid crystalline droplets. *Chem. Mater.* **2014**, *26*, 496−506.
(16) Jiang, J.; Yang, D. K. Bipolar to toroidal configuration transition in liquid crystal droplets. *Liq. Cryst.* **2018**, *45*, 102−111.
(17) Chen, H. Q.; Wang, X. Y.; Bisoyi, H. K.; Chen, L. J.; Li, Q. Liquid crystals in curved confined geometries: microfluidic bring new capabilities for photonic applications and beyond. *Langmuir* **2021**, *37*, 3789−3807.
(18) Wei, W. S.; Xia, Y.; Ettinger, S.; Yang, S.; Yodh, A. G. Molecular heterogeneity drives reconfigurable nematic liquid crystal drops. *Nature* **2019**, *576*, 433−436.
(19) Dan, A.; Aery, S.; Zhang, S.; Baker, D. L.; Gleeson, H. F.; Sarkar, A. Protein Microgel-stabilized pickering liquis crystal emulsions undergo analyte-triggered configurational transition. *Langmuir* **2020**, *36*, 10091−10102.
(20) Erdmann, J. H.; Žumer, S.; Doane, J. W. Configuration transition in a nematic liquid crystal confined to a small spherical cavity. *Phys. Rev. Lett.* **1990**, *64*, 1907−1910.
(21) Wei, W. S.; Jeong, J.; Collings, P. J.; Yodh, A. G. Focal conic flowers, dislocation rings, and undulation textures in smectic liquid crystal Janus droplets. *Soft Matter* **2022**, *18*, 4360−4371.
(22) Jeong, J.; Gross, A.; Wei, W. S.; Tu, F.; Lee, D.; Collings, P. J.; Yodh, A. G. Liquid crystal Janus emulsion droplets: preparation, tumbling, and swimming. *Soft Matter* **2015**, *11*, 6747−6754.
(23) Concellón, A.; Zentner, C. A.; Swager, T. M. Dynamic complex liquid crystal emulsions. *J. Am. Chem. Soc.* **2019**, *141*, 18246−18255.
(24) Urbanski, M.; Reyes, C. G.; Noh, J. H.; Sharma, A.; Geng, Y.; Jampani, V. S. R.; Lagerwall, J. P. F. Liquid crystals in micron-scale droplets, shells and fibers. *J. Condens Matter. Phys.* **2017**, *29*, 133003.
(25) Goyal, R. K.; Denn, M. M. Surface-Induced morphology and free-energy pathways in breakup of a nematic liquid crystalline cylinder. *Phys. Rev. E* **2008**, *78*, 021706.
(26) Lagerwall, J. P. F.; McCann, J. T.; Formo, E.; Scalia, G.; Xia, Y. Coaxial electrospinning of microfibers with liquid crystal in the core. *Chem. Commun.* **2008**, *42*, 5420−5422.
(27) Matthias, H.; Schweizer, S. L.; Wehrspohn, R. B.; Kitzerow, H. S. Liquid crystal director fields in micropores of photonic crystals. *J. Opt. Pure Appl. Opt.* **2007**, *9*, S389.
(28) Svetec, M.; Slavinec, M. Structural transition of nematic liquid crystals in cylindrical capillary as a result of the annihilation of two point defects. *Chem. Phys.* **2008**, *128*, 084704.
(29) Pairam, E.; Vallamkondu, J.; Koning, V.; van Zuiden, B. C.; Ellis, P. W.; Bates, M. A.; Vitelli, V.; Fernandez-Nieves, A. Stable nematic droplets with handles. *Proc. Natl. Acad. Sci. U.S.A.* **2013**, *110*, 9295−9300.
(30) Javadi, A.; Eun, J.; Jeong, J. Cylindrical nematic liquid crystal shell: effect of saddle-splay elasticity. *Soft Matter* **2018**, *14*, 9005−9011.
(31) Liang, H. L.; Noh, J. H.; Zentel, R.; Rudquist, P.; Lagerwall, P. F. Tuning the defect configurations in nematic and smectic liquid crystals shells. *Philos. Trans. R. Soc.* **2013**, *371*, 20120258.
(32) Lopez-Leon, T.; Fernandez-Nieves, A.; Nobili, M.; Blanc, C. Nematic-smectic transition in spherical shells. *P. R. Libre* **2011**, *106*, 247802.
(33) Xia, Y.; Lee, E.; Hu, H.; Gharbi, M. A.; Beller, D. A.; Fleischmann, E. K.; Kamien, R.; Zentel, S.; Yang, S. Better actuation through chemistry: using surface coating to create uniform director fields in nematic liquid crystal elastomers. *ACS Appl. Mater. Interfaces* **2016**, *8*, 12466−12472.
(34) Drzaic, P.; Drzaic, P. S. Putting liquid crystal droplets to work: a short history of polymers dispersed liquid crystals. *Liq. Cryst.* **2006**, *33*, 1281−1296.
(35) Mukai, K.; Hara, M.; Yabu, H.; Nagano, S.; Seki, T. Photoswitchable configuration of nematic liquid crystal droplets embedded in a honeycomb-patterned film. *Adv. Mater. Interfaces* **2021**, *8*, 2100891.
(36) Kitzerow, H. Polymer-dispersed liquid crystals: from the nematic curvilinear aligned phase to ferroelectric films. *Liq. Cryst.* **1994**, *16*, 1−31.
(37) Kamal, W.; Li, M.; Lin, J.; Parry, E.; Jin, Y.; Elston, S. J.; Castrejón-Pita, A. A.; Morris, S. M. Spatially patterned polymer dispersed liquid crystals for image integrated smart windows. *Adv. Opt. Mater.* **2022**, *10*, 2101748.
(38) Natarajan, L. V.; Shepherd, C. K.; Brandelik, D. M.; Sutherland, R. L.; Chandra, S.; Tondiglia, V. P.; Tomlin, D.; Bunning, T. J. Switchable holographic polymer-dispersed liquid crystal reflection gratings based on thiol− ene photopolymerization. *Chem. Mater.* **2003**, *15*, 2477−2484.
(39) Aphonin, O. A.; Panina, Y. V.; Pravdin, A. B.; Yakovlev, D. A. Optical properties of stretched polymer dispersed liquid crystal films. *Liq. Cryst.* **1993**, *15*, 395−407.
(40) Zhao, Y.; Bai, S.; Banh, T. N.; Brazeau, J. Orientation and anchoring effects in stretched polymer dispersed nematic liquid crystals. *Liq. Cryst.* **2000**, *27*, 1183−1187.
(41) Cairns, D. R.; Bowley, C. C.; Danworaphong, S.; Fontecchio, A. K.; Crawford, G. P.; Li, L.; Faris, S. M. Optical strain characteristics of holographically formed polymer-dispersed liquid crystal films. *Appl. Phys. Lett.* **2000**, *77*, 2677−2679.
(42) Prishchepa, O. O.; Shabanov, A. V.; Zyryanov, V. Y.; Parshin, A. M.; Nazarov, V. G. Friedericksz threshold field in bipolar nematic droplets with strong surface anchoring. *JETP Lett.* **2007**, *84*, 607−612.
(43) Fu, F.; Abukhdeir, N. M. Formation and field-driven dynamics of nematic spheroids. *Soft Matter* **2017**, *13*, 4890−4902.

https://doi.org/10.1021/acs.langmuir.2c02461
Langmuir 2022, 38, 15272−15281

(44) Khayyatzadeh, P.; Fu, F.; Abukhdeir, N. M. Field-driven dynamics of nematic microcapillaries. *Phys. Rev. E* **2015**, *92*, 1−10.
(45) Krakhalev, M. N.; Prishchepa, O. O.; Sutormin, V. S.; Zyryanov, V. Y. Director configurations in nematic droplets with tilted surface anchoring. *Liq. Cryst.* **2017**, *44*, 355−363.
(46) Jeong, J.; Kim, M. W. Confinement-induced transition of topological defects in smectic liquid crystals: from a point to a line and pearls. *Phys. Rev. Lett.* **2012**, *108*, 1−5.
(47) Jeong, J.; Kim, M. W. Observation of liquid crystals confined in an elliptic cylinder. *Appl. Phys. Lett.* **2012**, *101*, 061914.
(48) Goyal, R. K.; Denn, M. M. Orientational multiplicity and transitions in liquid crystalline droplets. *Phys. Rev. E* **2007**, *75*, 021704.
(49) Pathak, G.; Grahari, K.; Yadav, G.; Srivastava, A.; Strzezysz, O.; Manohar, R. Tuning of birefringence, response time, and dielectric anisotropy by the dispersion of fluorescent dye into the nematic liquid crystal. *Appl. Phys. A* **2018**, *124*, 1−9.
(50) Ravnik, M.; Žumer, S. Landau- de Gennes modeling of nematic liquid crystal colloids. *Liq. Cryst.* **2009**, *36*, 1201−1214.
(51) De Gennes, P. G.; Prost, J.; Pelcovits, R. *The Physics of Liquid Crystals*; Oxford University Press, 1993.
(52) Fournier, J. B.; Galatola, P. Modeling planar degenerate wetting and anchoring in nematic liquid crystals. *Europhys. Lett.* **2005**, *72*, 403−409.
(53) Ondris-Crawford, R.; Boyko, B. E.; Wagner, B. G.; Erdmann, J. H.; Žumer, S.; Doane, J. W. Microscope textures of nematic droplets in polymer dispersexd liquid crystals. *J. Appl. Phys.* **1991**, *69*, 6380−6386.
(54) Chiccoli, C.; Evangelista, L. R.; Pasini, P.; Skačej, G.; Teixeira de Souza, R. T.; Zannoni, C. On the defect structure of biaxial nematic droplets. *Sci. Rep.* **2018**, *8*, 2130.
(55) Designolle, V.; Herminghaus, S.; Pfohl, T.; Bahr, C. AFM study of defect-induced depressions of the smectic-A/air interface. *Langmuir* **2006**, *22*, 363−368.
(56) Yu, B.; Li, B.; Jin, Q.; Ding, D.; Shi, A. C. Confined self-assembly of cylinder-forming diblock copolymers: effects of confining geometries. *Soft Matter* **2011**, *7*, 10227−10240.
(57) Chi, P.; Wang, Z.; Li, B.; Shi, A. C. Confinement-induced morphologies of diblock copolymers. *Langmuir* **2011**, *27*, 11683−11689.

https://doi.org/10.1021/acs.langmuir.2c02461
Langmuir 2022, 38, 15272−15281